Challenges in Acquiring Clinical Simultaneous SPECT-MRI on a PET-MRI Scanner

Ashley J. Morahan, Ilenia D'Adda, *Member, IEEE*, Kjell Erlandsson, *Member, IEEE*, Marco Carminati, *Senior Member, IEEE*, Marilena Rega, Darren Walls, Carlo Fiorini, *Senior Member, IEEE*, Brian F. Hutton, *Senior Member, IEEE*

Abstract—The INSERT is the world's first clinical SPECT-MRI brain imaging system based on scintillation detectors with a SiPM readout. Here we demonstrate its use within a clinical MRI environment for the first time. Using a standard transmit-receive head coil, and with an appropriate selection of a custom MRI sequence (GRE), we overcome mutual interference. The INSERT and its bulky 50 kg tungsten collimator introduce magnetic field inhomogeneity. Due to the specific MRI-compatible collimator design, inhomogeneity is compensated by shimming, leading to simultaneous acquisition. We process the SPECT data acquired alongside the MRI sequence to evaluate the SPECT system performance and the impact of the MRI. Finally, we present a set of simultaneous SPECT-MRI acquisitions, demonstrating multimodal imaging capabilities, albeit with a limited MRI sequence.

Index Terms—SPECT, MRI, SiPM, CsI(Tl), Clinical, Multimodal Imaging.

I. INTRODUCTION

THE development of multi-modal imaging has resulted in many benefits to the field of nuclear medicine [1]. The ability to combine two imaging modalities provides mutual improvement to functional and structural imaging methods. The available images of biological processes obtained from SPECT and PET can be complemented by the high-resolution structural images obtained through CT or MRI scans, improving diagnostics and treatment planning. Combined modalities provide practical advantages for the clinic as the time and space needed for a patient scan are reduced. There are challenges with developing a simultaneous scanning system, particularly with compatibility between systems and costs. Many clinics use combined scans such as SPECT-CT or PET-CT, and more recently PET-MRI [2]. However, clinical SPECT-MRI systems have not yet been established due to the technical challenges that face the combination of these systems. In this paper, we explore the implementation of the clinical SPECT-MRI INSERT (INtegrated SPECT/MRI for Enhanced stratification of brain tumours in Radio-chemoTherapy) for the first time within a clinical MRI environment.

Multiple clinical scenarios benefit from combining information from two imaging modalities [3]: this could be carried out with two separate systems, a single sequential imaging system, or a single simultaneous system. Separate systems take the most time and space, and the images have no temporal or spatial registration. Also, physical or biological changes may occur in between scans as they may be carried out on separate days. A sequential system reduces procedure time and clinical space significantly, but may still require image registration. A simultaneous system is able to acquire both images with temporal and spatial registration. SPECT-CT and PET-CT scans have proven to be successful in diagnostics and therapeutic studies [4], as CT images can be used to correct for attenuation and provide an anatomical image to aid the reconstruction of the SPECT or PET images. Combined imaging is advantageous in the diagnosis and monitoring of tumours or infections, as a radio-pharmaceutical can highlight metabolic and biological functions with high sensitivity, while CT and MRI provide a high-resolution anatomical image to localise abnormal tissue. These advantages have been achieved with PET-MRI systems which have been established through the development of MRI-compatible PET detectors [5]. MRI has the advantage over CT as it provides no radiation dose to the patient and has a range of imaging capabilities beyond anatomical images. The MRI is capable of chemical and functional imaging through versatile techniques such as diffusion-weighted imaging (DWI) [6], functional MRI (fMRI) [7], and spectroscopy [8]. Soft tissue brain imaging is particularly advantageous in MRI systems.

SPECT-MRI systems have not yet been established partly due to the potential incompatibility issues between the systems. The three primary issues with MRI compatibility of a SPECT scanner are: (i) the gamma camera electronics, (ii) the detector motion within the MRI bore and (iii) the presence of paramagnetic collimators. The first of these challenges have been solved in PET-MRI systems, but the latter is yet to be established in clinical SPECT scanners.

Traditional gamma cameras use photomultiplier tube (PMT) based detectors which cannot operate within an MRI environment. This is overcome in PET-MRI with the use of solid-state readout, which can operate in a magnetic field. Solid-state technologies can be expensive alternatives but have also proved to be advantageous in stand-alone PET systems: silicon photomultiplier (SiPM) based systems have improved

spatial resolution and superior time resolution [9] [10] for time-of-flight (ToF) PET. Some preclinical SPECT systems have adopted alternative solid-state technology (cadmium zinc telluride (CZT) detectors), [11], [12], but no clinical detectors have been designed with MRI compatibility in mind.

Most SPECT systems make use of a rotating gantry to acquire the necessary angles for tomographic reconstruction. Motion during an MRI acquisition can cause artefacts to arise in the image. To capture the multiple angles with a stationary system, many detector heads must be used, increasing the cost and complexity of the SPECT system. A SPECT-MRI system must be inherently stationary.

A vital component in SPECT is the collimator which usually consists of a large piece of lead or tungsten which causes issues in the MRI as the static magnetic field (B_0) must compensate for its presence. The heavy bulk causes inhomogeneity in the static magnetic field that reduces image quality. The shim coils are able to correct the inhomogeneity through field shimming; however, the fast switching gradient magnetic fields can induce eddy currents in metallic components inside the MRI bore. An ideal MRI-compatible collimator will induce no eddy currents and maintain B_0 homogeneity.

There have been developments in preclinical SPECT-MRI systems [13], [14]. These systems are limited by the small bore size and imaging field-of-view (FoV), suitable for preclinical imaging systems, but the principle has not been expanded to a larger system for clinical use. In this paper, we establish the use of a clinical SPECT system designed for the simultaneous acquisition of MRI data. The novel system is evaluated, and the challenges faced in this SPECT-MRI operation are addressed.
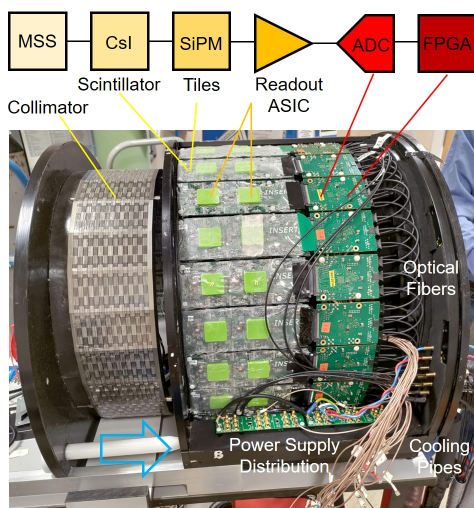

Fig. 1. Block scheme of the detector components and picture of the open scanner with the MSS collimator extracted from its location in front of the ring of 20 detection modules.

II. MATERIALS AND METHODS

The INSERT is the world's first clinical SPECT brain imaging system, designed with SiPM readout for integration with clinical MRI systems [15]. To overcome the challenges in SPECT-MRI compatibility, the scanner is comprised of a stationary partial ring of 20 MRI-compatible detectors with a novel collimator design. The architecture of the detector is pictured in Fig. 1. Each detector head comprises an 8 mm thick, monolithic, 10 cm × 5 cm Thallium-activated Caesium Iodide (CsI: Tl) crystal coupled with a custom-built SiPM (by FBK, Italy) readout array of 72 pixels per module (1440 photodetectors in total) [16]. The SiPM signals are read by two 36-channel programmable ASICs named ANGUS and developed for this project [17]. The module electronics (visible in Fig. 1) are composed of two printed circuit boards (PCB): the analogue board hosts the ASICs and the connectors to the SiPM tiles. The latter is separated from the board by the cooling block (printed in a special thermally conductive plastic). The second board is the DAQ board hosting the ADC digitising the analogue signals, the FPGA and the optical transceivers. The boards, arranged in a modular and tiled layout, are designed according to mutual compatibility design guidelines [18], in terms of PCB layout and choice of components, which make them compatible with MRI, preventing, for instance, eddy current induction and sensitivity to gradients. Acquired data are digitised and transferred via optical fibres to an external network gateway of the daisy chain, keeping all non-MRI-compatible components behind a shielded filter plate.

The INSERT scanner makes use of a novel multi-slit-slat (MSS) collimator [19], designed to acquire a 20 cm trans-axial diameter by 9 cm axial usable FoV within the compact MRI bore. It is composed of more than 6,000 plates and weighs about 50 kg. This design is suitable for brain imaging and is able to accommodate an MRI head coil. The novel slit-slat collimator is comprised of slits internal to the slat length to achieve trans-axial minimisation without compromising the slat length that defines axial resolution. The tungsten collimator is built with thousands of individually isolated pieces, preventing the induction of eddy currents. The stationary design uses minification and high intrinsic resolution detectors to acquire the necessary data for tomographic reconstruction, [20]. The MRI compatibility of all electronic components (except for the collimator) was verified on a preclinical system where boards have the clinical form factor but are 50% populated and only 10 modules are daisy-chained [21]. The complete clinical system has undergone initial testing as a stand-alone SPECT scanner [22], [23].

The INSERT design considerations allow the SPECT components to operate within the MRI environment; however, there are still issues that arise. The bulk of the clinical system can affect field homogeneity, and the presence of electrical signals can interfere with normal MRI operation. Here we set out to determine which MRI protocols are able to operate

Fig. 2. The INSERT clinical system (44 cm diameter, 28 cm of internal bore) placed in the bore of the Siemens PET-MR system for simultaneous scanning. The dual-tuned head coil resides within the INSERT bore (26.5 cm internal bore) and holds an MRI phantom. The cooling pipes, electrical wires and optical fibres pass through the back of the bore and connect to an external room via filter plates and waveguides.

during the acquisition of SPECT data. The INSERT was installed in a Siemens Biograph mMR [24], with a 2.89 T static magnetic field (Fig. 2). A customised birdcage-shielded transmit/receive radio frequency (RF) coil was designed for the preclinical prototype of the SPECT scanner, whose mutual compatibility with MRI was successfully demonstrated [18]. In this case, a 3T Dual Tuned Quadrature Head Coil (by Rapid Biomedical GmbH, Rimpar, Germany) was used to acquire MRI data. The INSERT was installed within a PET-MRI system to comply with radiation protection and safety requirements at University College Hospital (London, UK). Installing the INSERT and using radiation within a standard clinical MRI room would require custom-built radiation shielding and safety procedures, which were not available. The electrical power supply, cooling pump, and operation station (laptop and communication gateway) were located outside of the scanning room and internal to the Faraday cage shielding. This kept all incompatible components far from the MRI and behind the shielding. The optical fibres, electrical wires and cooling pipes passed through waveguides and filter plates to connect to the INSERT within the scanning room. The INSERT is loaded into the back of the PET-MRI bore, with all cables away from the patient bed. This is a practical and safe implementation of the SPECT scanner with minimum interference with the patient or the existing PET-MRI system.

A. MRI Performance

We set out to assess the quality of the MRI performance when operated alongside the INSERT. Here the MRI field homogeneity and image SNR are quantified as a measure of MRI performance. Measurements of a uniform spherical phantom (18 cm diameter sphere, filled with mineral oil) were taken in three configurations in the MRI: inside the TX/RX head coil only, and then inside the TX/RX head coil within the INSERT (with and without power).

Field Homogeneity:

The magnetic field homogeneity is defined by the uniformity of the magnetic field (B_0) in the centre of the bore when no patient is present [25]. The presence of large or metallic objects or external electromagnetic fields around or in the MRI bore will reduce homogeneity. The primary source of inhomogeneity is caused by the scanner's permanent surroundings, pipes, wires and external fields. During installation, the MRI is fitted with ferromagnetic components which correct the B_0 field for any permanent external interference. After this, all other sources of inhomogeneity must be corrected with active shimming.

An ideal homogeneous field will present a delta function at $\omega_0 = 123.2\ MHz$ for a 2.89 T magnet. To measure the field inhomogeneity, a B_0 field mapping must be acquired [26]. The mapping is based on a multi-spin echo sequence, here two spin echos are used. The deviation from ω_0 is given by the dephasing between the echos, $\delta\omega$, the average measurement in the field mapping corresponds to inhomogeneity in the FoV. By assuming $\delta\omega$ is solely due to variation in B_0 we can define Eqn. 1 [27].

$$\delta\omega = \frac{\phi(TE_2)\phi^*(TE_1)}{2\pi(TE_2 - TE_1)} \tag{1}$$

where the phase, ϕ, and its transpose are given for each spin echo and their corresponding echo times, TE.

Acquisitions were taken with shimming, to give a measure of the expected homogeneity during simultaneous acquisitions. The INSERT collimator is designed to prevent eddy currents, allowing for safe active shimming. The baseline homogeneity was compared with that of the INSERT in the bore (power off) and during SPECT acquisition (power on).

Electronic Noise in MRI Sequences:

The second experiment aimed to measure the impact of electrical noise from the SPECT detectors. The presence of external electrical signals can increase the noise in the MRI and cause image artefacts due to unwanted signals in the frequency domain. MRI sequences can account for reduced SNR by increasing signal in several ways [28], increasing the number of acquisitions for averaging, choosing a larger FoV, increasing the slice thickness, optimising the repetition time (TR), reducing the acquisition matrix size (larger voxels) and/ or choosing a shorter echo time (TE).

The MRI sequences available on the Siemens system were tested with the INSERT in the bore. We selected sequences which would be suitable for use in brain imaging and identified those which could compensate for the loss of signal and the presence of electronic noise. From these sequences, four produced suitable images for use alongside SPECT imaging, namely: the T2 weighted turbo spin echo (TSE) and gradient echo (GRE) sequences and T1 weighted

TABLE I
MRI SEQUENCE PARAMETERS. ST: SLICE THICKNESS. NSA: NUMBER OF SIGNAL AVERAGES. ETL: ECHO TRAIN LENGTH

Sequence	TR (ms)	TE (ms)	Flip Angle (°)	Pixel size (mm)	FoV (px)	ST (mm)	NSA	ETL
Field Mapping	400	7.65	60	3.40	64x60	3	1	N/A
TSE (T2)	3500	18	150	1.73	192x156	4.5	1	7
GRE (T2)	485	15	30	0.72	320x320	5	2	N/A
GRE (T1)	350	4.56	90	0.85	384x384	5	1	N/A
MPRAGE (T1)	1800	3.01	9	0.28	816x512	1	1	N/A

magnetisation prepared rapid acquisition gradient echo (MPRAGE) and GRE sequences (Tab. I). The spherical phantom was imaged with each sequence while the INSERT was powered, and the SNR was calculated: $SNR = \frac{S}{\eta}$ where the average signal (S) was measured inside of an 80% region of interest within the phantom (the ROI mask covered 14.4 cm of the phantom diameter) and background (η) outside the phantom.

B. SPECT Performance

Here we assess the impact of the MRI on the SPECT system. The use of the SPECT within an MRI environment poses complications due to the strong magnetic fields and fast switching RF signals. As discussed, this has been accounted for in the INSERT design and verified in the preclinical design. Here we assess the clinical system for the first time in the MRI.

The performance of the INSERT is evaluated within the MRI scanner before and during an imaging sequence. A 21 cm (D)× 18 cm (L) cylindrical phantom with 13 fillable 1.4 cm (D)× 10 cm (L) cylindrical rods was used in the following experiments (Fig. 3). This phantom was chosen for its MRI compatibility and suitable size within the SPECT bore. Nine radioactive rods were placed in a 3×3 matrix, columns 2.5 cm apart and rows 4 cm apart. The rods were filled with concentrations of 0.46, 0.93, and 1.40 MBq/mL of ^{99m}Tc. Three scans were acquired, such that each activity concentration was placed at each of the nine positions in the phantom, giving a measurement of each activity across the SPECT FoV. Each configuration was measured outside of the PET-MRI and repeated inside the PET-MRI during the imaging sequence.

The SPECT images were reconstructed using the maximum likelihood - expectation maximisation (ML-EM) algorithm (Eqn. 2) [29]. ML-EM reconstruction calculates activity distribution, θ_j^{k+1}, from the measured data, m_i, and system model, a_{ij}. The noise term, η, includes sources of background counts. The events used in the reconstruction are taken from a ±10% energy window at the 140 keV photopeaks.

$$\theta_j^{k+1} = \frac{\theta_j^k}{\sum_i a_{ij}} \sum_i^I m_i \frac{a_{ij}}{\sum_{d=1}^J a_{id}\theta_d^k + \eta} \qquad (2)$$

Specific issues due to the PET detectors:
Although the INSERT is designed for use in a clinical MRI system, the Biograph mMR is a PET-MRI system. The
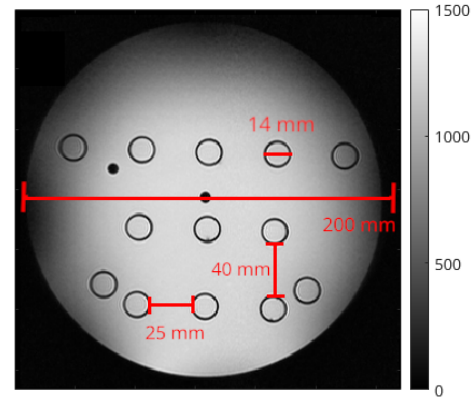

Fig. 3. The quality of the SPECT and MRI were established with a cylinder phantom. The four outermost rods were filled with water and had no activity concentration. This image was captured with the T2 GRE sequence.

presence of the radioactive Lutetium isotope ^{176}Lu in the PET $Lu^2SiO_5 : Ce(LSO)$ detectors poses an additional problem for the SPECT system, as background counts are emitted at the 88, 202 and 307 keV decay peaks (Fig. 4). A significant contribution from the background counts would reduce image quality. We assess the impact of ^{176}Lu emission during data acquisition and seek to remove its contribution.

The ^{176}Lu could pose two potential problems in the SPECT acquisition: the increase of background counts in the image and a possible limit on high count-rate performance. The LSO detectors covered 200 mm in the axial direction and were aligned with the isocentre of the MRI; therefore, the LSO overlapped with the SPECT detectors during the simultaneous scan. The ^{176}Lu contribution was measured by acquiring a background scan with the INSERT whilst inside the PET-MRI bore. The background was measured three times for 10 minutes each to assess the expected contribution from ^{176}Lu during a SPECT-MRI scan. The measured count rate of the ^{176}Lu emission was not high enough to introduce a significant dead time in the detectors. The existing lead shielding around the SPECT detectors also reduces the ^{176}Lu counts.

The ^{176}Lu background measurement is used to model the background term in the ML-EM algorithm. The measurement is scaled for the SPECT acquisition time and included in the additive term, η. The cylinder phantom data were reconstructed with the updated algorithm. The activity concentration was calculated by the sum of counts in each rod and accounting for decay over time and prepared dose.
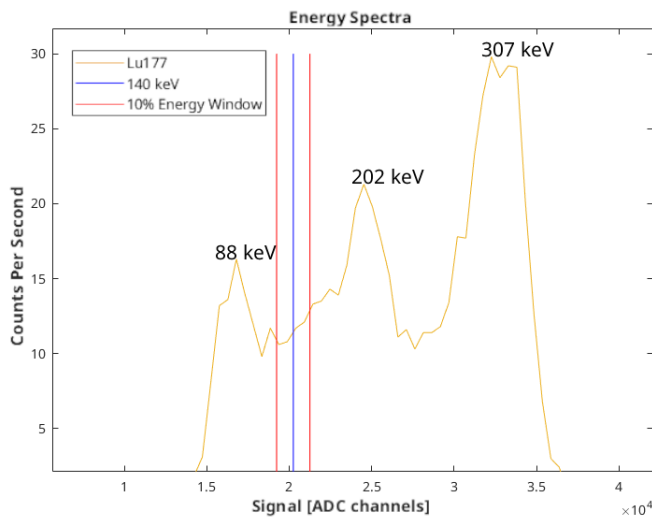
Fig. 4. Energy spectrum for one 10 minute background acquisition of ^{176}Lu in the INSERT system. The ^{99m}Tc energy window (10 % at 140 KeV) is also shown.

The average counts as a function of activity are plotted, and a linear fitting is calculated to determine the measure of activity linearity in the reconstructed images. The coefficient of variation ($CoV = \frac{\sigma}{\mu}$) is measured in each cylinder, where μ is the average reconstructed counts between the 9-rod positions for each activity concentration, and σ is the corresponding standard deviation. Here the system uniformity is classified by the CoV values across each cylinder position in the FoV.

C. Simultaneous SPECT-MRI

The benefits of MRI-assisted SPECT imaging were explored with the cylinder phantom, with the same nine filled rods of ^{99m}Tc. The image was acquired simultaneously on both systems. The SPECT and MRI acquisitions were set to the same acquisition time, totalling 5 minutes. The MRI acquisition was restricted to the SPECT detector FoV; the MRI isocentre was aligned with the centre of the SPECT detectors, and the axial FoV was limited to the 9 cm detector size. The SPECT image was reconstructed with a matching 0.72 mm voxel size and FoV to that of the 320x320 MR image. The separate MRI and SPECT systems require alignment, carried out by using the positions of the rod centres to perform a rigid spatial registration.

The INSERT partial ring design has been reported previously as a limitation in the SPECT system, [23]. The reduced sampling in the partial detector ring can be overcome through a $> 70°$ phantom rotation and performing a second SPECT acquisition in order to sample data in the missing angles. The motion can be difficult to measure in the SPECT image alone. Reconstructing the SPECT image with 20 sampling angles or fewer is referred to here as partial ring reconstruction (PRR). Performing a rotation to acquire at least 25 angles to completely sample the FoV is called full ring reconstruction (FRR). The rotated positions were transformed, and tomo-

graphic image reconstruction was carried out with 50 iterations of an ML-EM algorithm, the image FoV is 20 cm × 20 cm.

With the acquisition of simultaneous SPECT-MRI data, the MRI images can be used to aid the reconstruction process. A SPECT-to-MRI registration provides a transformation between the two acquisitions which is used to combine the SPECT data from the two angular acquisitions. The higher contrast and structure in the MRI images ensure greater accuracy of the transformation compared to that of SPECT-to-SPECT alone.

The SPECT was further improved with the inclusion of an MRI-generated anatomical prior. The maximum a posteriori expectation maximisation algorithm (MAP-EM) [30] improves the SPECT reconstruction by introducing a penalty term based on anatomical structure. The MRI image of the phantom is separated into segments, defining the phantom boundaries and hot and cold regions within the phantom. A Gaussian filter is applied, constrained within these boundaries, to generate a prior image. The SPECT image is reconstructed with 80 iterations of the MAP-EM algorithm with the FWHM of the Gaussian smoothing filter set to 3.0 mm, and $\beta = 0.5$, the prior weighting factor.

III. RESULTS

A. MRI Performance

Magnetic Field Homogeneity

The B_0 field mapping produces a frequency domain measurement of the imaging FoV. Table II shows the average frequency bandwidth in each field mapping measurement. While the INSERT is in the bore (with power off), the frequency bandwidth is nearly double that of the baseline, a result of the loss in field homogeneity. As a result, there is a loss of signal in the acquired images. When the INSERT is powered, the homogeneity is further reduced and the presence of electrical noise is observed by the larger variance.

TABLE II
MEASUREMENTS TAKEN FROM THE B_0 FIELD MAPPING AND IMAGE SEQUENCES. $\delta\omega$ IS CALCULATED FROM THE MEAN FREQUENCIES WITHIN THE B_0 MAPPING. SNR IS CALCULATED FROM THE IMAGE OUTPUT OF EACH SEQUENCE WITH THE INSERT POWERED ON INSIDE THE BORE.

Field Mapping	$\delta\omega$ [Hz]
Baseline	56.98 ± 9.76
INSERT- No Power	105.09 ± 8.02
INSERT - Power	119.64 ± 18.11
Imaging Sequence	**SNR**
TSE (T2)	9.96
GRE (T2)	8.95
GRE (T1)	5.27
MPRAGE (T1)	0.29

Electrical Noise in MRI Sequences

The measurements of SNR (Tab. II) presented the greatest SNR in the TSE sequence. The high image quality and short acquisition times in TSE are advantageous in PET-MRI systems [31]; unfortunately, the TSE was unable to be acquired simultaneously with the INSERT. The initiation

of the TSE interfered with the DAQ boards and ceased the digital communication of the instrument. The TSE was reserved for use in sequential SPECT-MRI imaging until the problem was resolved.

A similar problem was found to occur in several MRI sequences. We believe without the correct shielding, the INSERT is unable to operate in the presence of certain levels of RF energy and waveforms, thus limiting the choice of MRI sequences which can be used for simultaneous scanning. The current RF coil was not shielded and so a suitable simultaneous imaging sequence was needed. The T2 weighted GRE sequence was found to be compatible with simultaneous INSERT acquisition.

GRE has a lower SNR than TSE; however, taking more signal averages can reduce the noise at the cost of longer acquisition time. Reducing matrix size and increasing slice thickness can also reduce noise. The small INSERT FoV is an advantage here, as the MRI FoV can be reduced to 20 cm × 20 cm × 10 cm to recover the signal with the GRE.

B. SPECT Performance

Fig. 5 demonstrates the result of measuring the activity concentration during a SPECT and SPECT-MRI scan. For the reasons outlined above, the MRI acquisition was limited to a GRE sequence. The comparison includes the effect of removing the ^{176}Lu counts from the reconstructed measurements. The baseline SPECT measurements display fewer counts than that of the SPECT-MRI (within the MRI bore). The relative difference is more significant in lower activity concentrations as the ^{176}Lu count rate is constant. Correcting for ^{176}Lu data reduces the background contribution and uncertainty in counts across the SPECT FoV. Once the ^{176}Lu is corrected, the INSERT performance within the PET-MRI is closer to that outside.

Table III presents the CoV of counts across all activity distributions. The CoV reduces when the ^{176}Lu is corrected. The measurements of counts are greatly affected by the position in the FoV, particularly in lower activity concentrations. This is due to the partial ring of detectors and the presence of an image artefact caused by the lost sampling angles. A straight line is fitted to the average counts, and Student's t-test is calculated to compare SPECT and SPECT-MRI data before and after ^{176}Lu correction. The R^2 in the slope is unchanged, suggesting the SPECT linearity has little variation during SPECT-MRI acquisitions. The difference between the SPECT and SPECT-MRI data was significant before ^{176}Lu correction ($p < 0.01$) but not significant after correction. The ^{176}Lu corrected SPECT-MRI images are not significantly different to the baseline SPECT images. The INSERT system has an image resolution of $< 1\ cm$ at the centre of the FoV [21]; the profile across the centre rods was plotted to determine the quality of the image during the GRE (Fig. 6). The INSERT performance

TABLE III
THE SIGNAL MEASUREMENTS ACROSS ACTIVITY CONCENTRATION TAKEN WITH AND WITHOUT SIMULTANEOUS MRI DEMONSTRATE THE LINEARITY IN THE INSERT SYSTEM.

Activity Conc. [MBq/mL]	COV		
	SPECT	SPECT-MRI	SPECT-MRI: ^{176}Lu Cor.
0.67	0.340	0.177	0.169
1.33	0.148	0.185	0.134
2.00	0.100	0.200	0.109
Modality	**Slope**	**Intercept**	**R^2**
SPECT	831.71	-176.97	0.99
SPECT-MRI	794.28	-33.27	0.99
SPECT-MRI: ^{176}Lu Cor	801.78	-84.93	0.99

is maintained during the GRE sequence after ^{176}Lu correction.
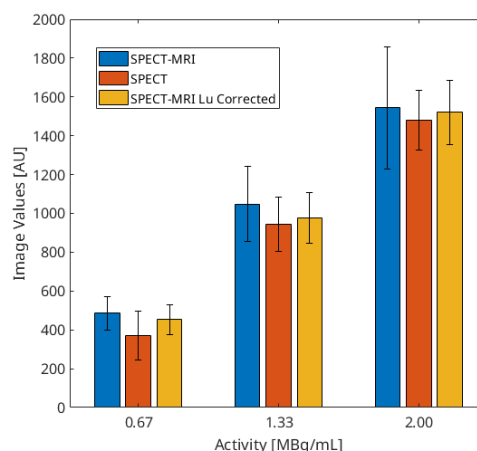

Fig. 5. Total counts within the ROI from 9 rod positions of 3 activity concentrations. The ^{176}Lu background was successfully removed, giving a comparable measurement to that outside of the MRI bore.

C. Simultaneous SPECT-MRI

Fig. 7 shows the results of the FRR and MAP-EM images compared to the standard PRR. Fig. 7(A) is reconstructed with a single SPECT acquisition, the partial ring has a gap of $70°$ where data are missing, this is seen by the loss of resolution at the bottom of the image. Fig. 7 (B) and (C) present the full ring reconstruction with 25 and 30 angles respectively. 25 detector angles represent a single full ring of detectors covering $360°$. The 30-detector reconstruction makes use of additional angles to further improve sampling.

Fig. 7 (D) presents the MAP-EM reconstruction applied to the cylinder phantom data, and FRR is applied alongside MAP-EM. The profiles in Fig. 8 show how the FRR is able to remove the reduced sampling artefact in the bottom of the image, and MAP-EM is able to regulate counts within the rods. The result in Fig. 9 demonstrates that the MAP-EM is able to reduce noise and align counts within the ROI defined by the MRI image.
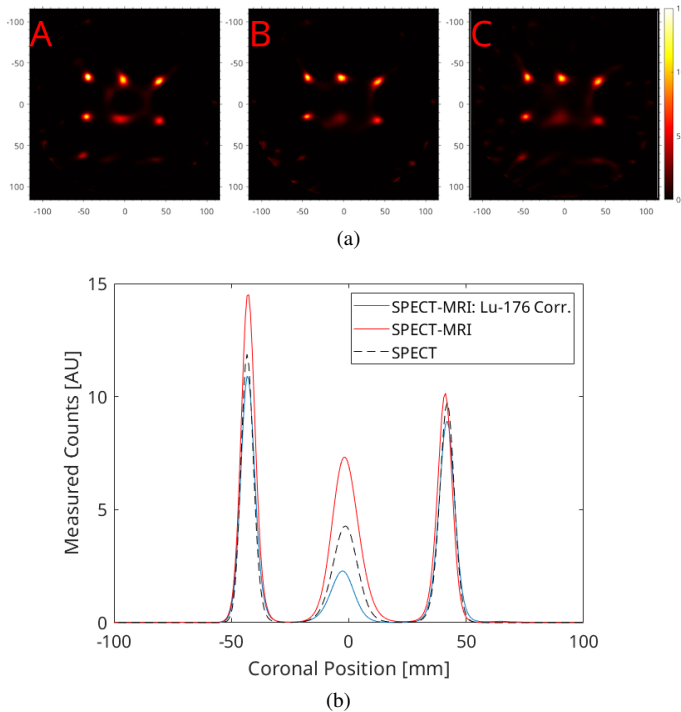
(a)

(b)

Fig. 6. (a) A: ML-EM image of 9 rods acquired outside of the MRI bore. B: Acquisition inside the MRI bore, ML-EM image has no ^{176}Lu modelling. C: ^{176}Lu modelling is included in the image reconstruction. Each image is scaled to the same colour bar. (b) The mean counts were taken from a coronal profile across the rods.

IV. DISCUSSION

The use of MRI with a bulky collimator has proved to be challenging for standard shimming procedures. Shimming in the presence of a large metallic object or induction loop such as copper can induce eddy currents which can damage the MRI coils. Also, we have had limitations in the use of an off-the-shelf RF coil which does not include shielding or support flexible tuning. Therefore we sought a sequence-based solution to improve SNR. The choice of MRI sequence can provide a high signal, however, some RF signals can pose a risk to the operation of SPECT electronics. A customised coil with appropriate shielding would allow more MRI sequences to be used safely alongside the SPECT and tuning of the coil could improve SNR in the MRI images, as we demonstrated with the preclinical version [21].

The presented results are based on experiments performed with the SPECT insert located in the bore of the gantry of a PET/MRI system. The main advantage was the avoidance of any additional radiation control in the experimental room since this is already designed for clinical use. The presence of background radiation from ^{176}Lu posed an additional challenge that would not be faced in a purely MRI system. A further limitation was the limited functionality of the MRI component of the dual-modality system. The reason for the failure of the SPECT acquisition is not clear and is the subject of an ongoing investigation. However, the results do suggest that the use of the INSERT in conjunction with

PET/MRI is feasible and may open further avenues for the investigation of tri-modality systems in which a sequential SPECT is performed following a simultaneous PET-MRI.

Of course, the use of CZT detectors can provide advantages in terms of energy resolution and compactness (no need for liquid cooling). Very interesting results, in particular with MRI-compatible preclinical SPECT inserts with high spatial resolution, have been achieved [32]. Unfortunately, the potential for that technology to scale up to clinical systems has not yet been demonstrated.

Although previous works have established PET-MRI compatibility, [31], [33], none have used MRI imaging with a clinical SPECT system. PET-MRI systems have demonstrated the compatibility of SiPM [34], however, through the addition of collimator compatibility this paper provides a pathway towards complete SPECT-MRI compatibility. Achieving MRI compatibility with a clinical SPECT collimator has not been previously demonstrated in any other scanner. The large collimator bulk has a significant effect on the performance of MRI and poses a risk of damaging the MRI coils. This has not been a problem for preclinical systems where much less bulky collimators can be used [13], [14], [35]. The intricate MSS collimator design has allowed the INSERT to acquire clinical SPECT images while maintaining MRI quality.

Improvements in the current INSERT performance are certainly possible. For instance, we have shown that improved event localisation via statistical depth of interaction (DOI) estimation in the monolithic crystal would be well suited to the novel MSS collimator, where the diverging slits can introduce uncertainty in localisation [36]. The use of MRI has aided in SPECT reconstruction and overcome the limitations of the INSERT design. MAP-EM reconstruction was successfully implemented and improved SPECT image quality by using the MRI. The FRR can improve the final SPECT images however, a similar acquisition may be difficult to implement in patient studies.

V. CONCLUSION

This body of work set out to achieve the first use of a simultaneous clinical SPECT-MRI system. We have successfully demonstrated the capabilities of the INSERT system and the sequences required for the MRI to function alongside the SPECT system. Although SPECT-MRI images were successfully acquired, this study is limited by the use of a single MRI sequence. Previous works have used shielding and customised RF coils to overcome RF interference, [37], [38], and we seek similar solutions for future work. The selected imaging protocol was able to overcome electrical interference and field inhomogeneity, so as to enable simultaneous acquisition albeit with a limited choice of MRI sequence. These preliminary results show promising developments in the field of SPECT-MRI.
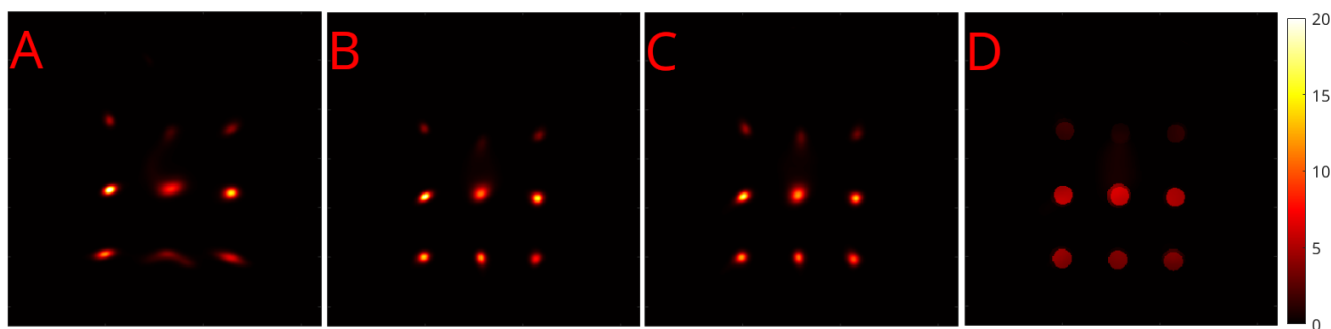
Fig. 7.　SPECT image reconstruction was driven by the simultaneous MRI acquisition. (A) SPECT acquisition acquired from a single scan of the INSERT system. (B) The reconstruction uses two acquisition positions to cover the detector gap and recover the resolution at the bottom of the image with 25 angles. (C) The SPECT reconstruction can use additional detector positions to acquire 30 detector angles, and the SPECT to MRI transformation registers all data in one space. (D) The MRI data provides anatomical prior to carrying out the MAP-EM reconstruction.
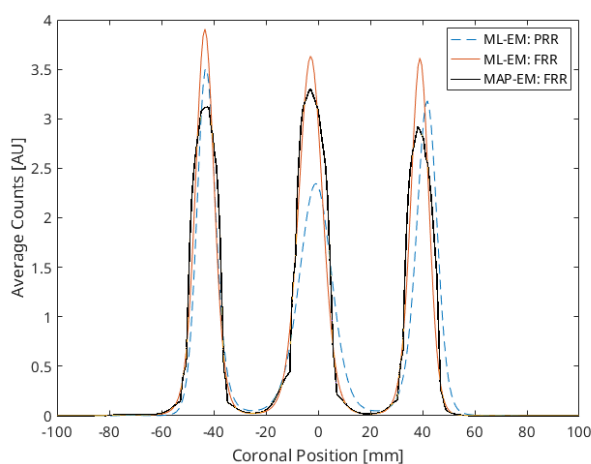

Fig. 8.　Profiles of the cylinder phantom rods reconstructed with ML-EM (PRR and FRR), and MAP-EM (FRR).
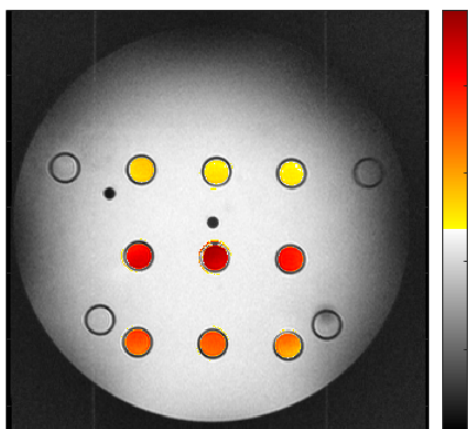

Fig. 9.　Combined SPECT-MRI data, simultaneously acquired. The colour map shows MRI in the bottom half (greyscale) and SPECT on top (colour scale). SPECT data were acquired for 5 minutes during the GRE sequence. The cylinder phantom covers the 200 mm diameter FoV, with 14 mm diameter rods shown by the dark rings. The colour bar presents arbitrary units used to scale the images for presentation.

REFERENCES

[1] J. A. Patton, D. W. Townsend, and B. F. Hutton, "Hybrid imaging technology: From dreams and vision to clinical devices," *Seminars in Nuclear Medicine*, vol. 39, no. 4, pp. 247–263, 2009, hybrid Imaging Anniversary Issue (Part I). [Online]. Available: https://www.sciencedirect.com/science/article/pii/S0001299809000191

[2] B. F. Hutton, K. Erlandsson, and K. Thielemans, "Advances in clinical molecular imaging instrumentation," *Clinical and Translational Imaging*, vol. 6, no. 1, pp. 31–45, 2018.

[3] O. Ratib and T. Beyer, "Whole-body hybrid PET/MRI: ready for clinical use?" *European journal of nuclear medicine and molecular imaging*, vol. 38, pp. 992–5, 04 2011.

[4] S. Cherry, "Multimodality imaging: beyond PET/CT and SPECT/CT," *Seminars in Nuclear Medicine*, vol. 39, no. 5, pp. 348–353, 2009.

[5] S. Vandenberghe and P. K. Marsden, "PET-MRI: a review of challenges and solutions in the development of integrated multimodality imaging," *Physics in Medicine and Biology*, vol. 60, no. 4, pp. R115–R154, feb 2015. [Online]. Available: https://doi.org/10.1088/0031-9155/60/4/r115

[6] K.-D. Merboldt, W. Hanicke, and J. Frahm, "Self-diffusion NMR imaging using stimulated echoes," *Journal of Magnetic Resonance (1969)*, vol. 64, no. 3, pp. 479–486, 1985. [Online]. Available: https://www.sciencedirect.com/science/article/pii/0022236485901118

[7] J. Lagopoulos, "Functional MRI: an overview," *Acta Neuropsychiatrica*, vol. 19, no. 1, p. 64–65, 2007.

[8] L. Vanhamme, T. Sundin, P. V. Hecke, and S. V. Huffel, "MR spectroscopy quantitation: a review of time-domain methods," *NMR in Biomedicine*, vol. 14, no. 4, pp. 233–246, 2001.

[9] J. van Sluis, J. de Jong, J. Schaar, W. Noordzij, P. van Snick, R. Dierckx, R. Borra, A. Willemsen, and R. Boellaard, "Performance characteristics of the digital biograph vision PET/CT system," *Journal of Nuclear Medicine*, vol. 60, no. 7, pp. 1031–1036, 2019. [Online]. Available: https://jnm.snmjournals.org/content/60/7/1031

[10] D. R. Schaart, G. Schramm, J. Nuyts, and S. Surti, "Time of flight in perspective: Instrumental and computational aspects of time resolution in positron emission tomography," *IEEE Transactions on Radiation and Plasma Medical Sciences*, vol. 5, no. 5, pp. 598–618, 2021.

[11] D. Wagenaar, O. Nalcioglu, L. Muftuler, D. Meier, K. Parnham, M. Szawlowski, M. Kapusta, S. Azman, J. Gjaerum, G. Maehlum, Y. Wang, B. Tsui, and B. Patt, "A multi-ring small animal CZT system for simultaneous SPECT/MRI imaging," *Journal of Nuclear Medicine*, vol. 48, no. supplement 2, pp. 89P–89P, 2007.

[12] D. Meier, D. J. Wagenaar, G. Mahlum, B. Sundal, B. E. Patt, S. Chen, J. Xu, J. Yu, B. M. Tsui, M. Hamamura *et al.*, "A SPECT camera for simultaneous SPECT/MRI," in *2009 IEEE Nuclear Science Symposium Conference Record (NSS/MIC)*. IEEE, 2009, pp. 2313–2318.

[13] D. Meier, D. Wagenaar, S. Chen, J. Xu, J. Yu, and B. Tsui, "A SPECT camera for combined MRI and SPECT for small animals," *Nuclear Instruments and Methods in Physics Research Section A: Accelerators, Spectrometers, Detectors and Associated Equipment*, vol. 652, no. 1, pp. 731–734, 2011, symposium on Radiation Measurements and Applications (SORMA) XII 2010. [Online]. Available: https://www.sciencedirect.com/science/article/pii/S0168900210021492

[14] L. Cai, X. Lai, Z. Shen, C.-T. Chen, and L. J Meng, "MRC-SPECT: A sub-500 μm resolution MR-compatible SPECT system for simultaneous dual-modality study of small animals." *Nuclear instruments & methods in physics research. Section A, Accelerators, spectrometers, detectors and associated equipment*, vol. 734 B, pp. 147–151, 2014.

[15] B. F. Hutton, M. Occhipinti, A. Kuehne, D. Máthé, N. Kovács, H. Waiczies, K. Erlandsson, D. Salvado, M. Carminati, G. L. Montagnani, S. C. Short, L. Ottobrini, P. van Mullekom, C. Piemonte, T. Bukki, Z. Nyitrai, Z. Papp, K. Nagy, T. Niendorf, I. de Francesco, and C. a. Fiorini, "Development of clinical simultaneous SPECT/MRI," *The British Journal of Radiology*, vol. 91, no. 1081, p. 20160690, 2018, pMID: 28008775. [Online]. Available: https://doi.org/10.1259/bjr.20160690

[16] M. Occhipinti, M. Carminati, P. Busca, A. Butt, G. Montagnani, P. Trigilio, C. Piemonte, A. Ferri, A. Gola, T. Bukki *et al.*, "Characterization of the detection module of the INSERT SPECT/MRI clinical system," *IEEE Transactions on Radiation and Plasma Medical Sciences*, vol. 2, no. 6, pp. 554–563, 2018.

[17] P. Trigilio, P. Busca, R. Quaglia, M. Occhipinti, and C. Fiorini, "A SiPM-readout ASIC for SPECT applications," *IEEE Transactions on Radiation and Plasma Medical Sciences*, vol. 2, no. 5, pp. 404–410, 2018.

[18] M. Carminati, G. L. Montagnani, M. Occhipinti, A. Kuehne, T. Niendorf, K. Nagy, A. Nagy, M. Czeller, and C. Fiorini, "SPECT/MRI INSERT compatibility: Assessment, solutions, and design guidelines," *IEEE Transactions on Radiation and Plasma Medical Sciences*, vol. 2, no. 4, pp. 369–379, 2018.

[19] D. Salvado, K. Erlandsson, A. Bousse, P. van Mullekom, and B. F. Hutton, "Novel collimation for simultaneous SPECT/MRI," in *2014 IEEE Nuclear Science Symposium and Medical Imaging Conference (NSS/MIC)*, 2014, pp. 1–5.

[20] M. Rogulski, H. Barber, H. Barrett, R. Shoemaker, and J. Woolfenden, "Ultra-high-resolution brain SPECT imaging: simulation results," *IEEE Transactions on Nuclear Science*, vol. 40, no. 4, pp. 1123–1129, 1993.

[21] M. Carminati, F. Baratelli, M. Occhipinti, K. Erlandsson, K. Nagy, Z. Nyitrai, M. Czeller, A. Kühne, T. Niendorf, S. Valtorta *et al.*, "Validation and performance assessment of a preclinical SiPM-based SPECT/MRI insert," *IEEE Transactions on Radiation and Plasma Medical Sciences*, vol. 3, no. 4, pp. 483–490, 2019.

[22] M. Carminati, I. D'Adda, A. J. Morahan, K. Erlandsson, K. Nagy, M. Czeller, B. Tölgyesi, Z. Nyitrai, A. Savi, P. van Mullekom, B. F. Hutton, and C. Fiorini, "Clinical SiPM-based MRI-compatible SPECT: Preliminary characterization," *IEEE Transactions on Radiation and Plasma Medical Sciences*, vol. 4, no. 3, pp. 371–377, 2020.

[23] A. J. Morahan, K. Erlandsson, I. D'Adda, M. Carminati, A. Savi, R.-M. Moresco, K. Nagy, Z. Nyitrai, B. Tolgyesi, D. Salvado, P. Van Mullekom, C. E. Fiorini, and B. F. Hutton, "Acquisition correction and reconstruction for a clinical SPECT/MRI insert," in *2019 IEEE Nuclear Science Symposium and Medical Imaging Conference (NSS/MIC)*, 2019, pp. 1–3.

[24] S. Øen, L. Aasheim, L. Eikenes, and A. Karlberg, "Image quality and detectability in siemens biograph PET/MRI and PET/CT systems—a phantom study," *EJNMMI Physics*, vol. 6, 08 2019.

[25] H. M. Gach, A. N. Curcuru, S. Mutic, and T. Kim, "B0 field homogeneity recommendations, specifications, and measurement units for mri in radiation therapy," *Medical Physics*, vol. 47, no. 9, pp. 4101–4114, 2020. [Online]. Available: https://aapm.onlinelibrary.wiley.com/doi/abs/10.1002/mp.14306

[26] H.-H. Chen, R. D. Boykin, G. D. Clarke, J.-H. T. Gao, and J. W. Roby III, "Routine testing of magnetic field homogeneity on clinical MRI systems," *Medical Physics*, vol. 33, no. 11, pp. 4299–4306, 2006. [Online]. Available: https://aapm.onlinelibrary.wiley.com/doi/abs/10.1118/1.2359229

[27] K. S. Nayak and D. G. Nishimura, "Automatic field map generation and off-resonance correction for projection reconstruction imaging," *Magnetic Resonance in Medicine*, vol. 43, no. 1, pp. 151–154, 2000.

[28] A. den Dekker and J. Sijbers, "Data distributions in magnetic resonance images: A review," *Physica Medica*,

vol. 30, no. 7, pp. 725–741, 2014. [Online]. Available: https://www.sciencedirect.com/science/article/pii/S1120179714000829

[29] L. A. Shepp and Y. Vardi, "Maximum likelihood reconstruction for emission tomography," *IEEE Transactions on Medical Imaging*, vol. 1, no. 2, pp. 113–122, 1982.

[30] E. Levitan and G. T. Herman, "A maximum a posteriori probability expectation maximization algorithm for image reconstruction in emission tomography," *IEEE Transactions on Medical Imaging*, vol. 6, no. 3, pp. 185–192, 1987.

[31] J. E. Mackewn, P. Halsted, G. Charles-Edwards, R. Page, J. J. Totman, K. Sunassee, D. Strul, W. A. Hallett, M. Jauregui-Osoro, P. Liepins, S. C. R. Williams, T. Schaeffter, S. F. Keevil, and P. K. Marsden, "Performance evaluation of an MRI-compatible pre-clinical PET system using long optical fibers," *IEEE Transactions on Nuclear Science*, vol. 57, no. 3, pp. 1052–1062, 2010.

[32] X. Lai, L. Cai, J.-W. Tan, E. M. Zannoni, B. Odintsov, and L.-J. Meng, "Design, performance evaluation, and modeling of an ultrahigh resolution detector dedicated for simultaneous SPECT/MRI," *IEEE Transactions on Radiation and Plasma Medical Sciences*, vol. 6, no. 1, pp. 42–50, 2022.

[33] J. Wehner, B. Weissler, P. M. Dueppenbecker, P. Gebhardt, B. Goldschmidt, D. Schug, F. Kiessling, and V. Schulz, "MR-compatibility assessment of the first preclinical PET-MRI insert equipped with digital silicon photomultipliers," *Physics in Medicine & Biology*, vol. 60, no. 6, p. 2231, feb 2015. [Online]. Available: https://dx.doi.org/10.1088/0031-9155/60/6/2231

[34] J. Wehner, B. Weissler, P. Dueppenbecker, P. Gebhardt, D. Schug, W. Ruetten, F. Kiessling, and V. Schulz, "PET/MRI insert using digital SiPMs: investigation of MR-compatibility," *Nuclear Instruments and Methods in Physics Research Section A: Accelerators, Spectrometers, Detectors and Associated Equipment*, vol. 734, pp. 116–121, 2014.

[35] R. Madru, P. Kjellman, F. Olsson, K. Wingårdh, C. Ingvar, F. Ståhlberg, J. Olsrud, J. Lätt, S. Fredriksson, L. Knutsson *et al.*, "99mTc-labeled superparamagnetic iron oxide nanoparticles for multimodality SPECT/MRI of sentinel lymph nodes," *Journal of Nuclear Medicine*, vol. 53, no. 3, pp. 459–463, 2012.

[36] I. D'Adda, A. J. Morahan, M. Carminati, K. Erlandsson, M. Ljungberg, B. F. Hutton, and C. Fiorini, "A statistical DOI estimation algorithm for a SiPM-based clinical SPECT insert," *IEEE Transactions on Radiation and Plasma Medical Sciences*, vol. 6, no. 7, pp. 771–777, 2022.

[37] P. Gebhardt, J. Wehner, B. Weissler, R. Botnar, P. Marsden, and V. Schulz, "FPGA-based RF interference reduction techniques for simultaneous PET-MRI," *Physics in Medicine & Biology*, vol. 61, no. 9, p. 3500, 2016.

[38] L. Yin, F. Schrank, N. Gross-Weege, D. Schug, and V. Schulz, "RF shielding materials for highly-integrated PET/MRI systems," *Physics in Medicine & Biology*, vol. 66, no. 9, p. 09NT01, Apr 2021. [Online]. Available: https://doi.org/10.1088/1361-6560/abf606